

Simulations of the Effects of Stripping and Accretion on Galaxy Haloes in Clusters.

David M. Acreman, Ian R. Stevens, Trevor J. Ponman, Irini Sakelliou

School of Physics and Astronomy, University of Birmingham, Edgbaston, Birmingham, B15 2TT, UK
Email: da@star.sr.bham.ac.uk, irs@star.sr.bham.ac.uk, tjp@star.sr.bham.ac.uk, irini@star.sr.bham.ac.uk

Accepted; Received; in original form

ABSTRACT

We present results from a series of hydrodynamic simulations investigating ram pressure stripping of galactic haloes as the host galaxy falls radially into a cluster. We perform a parameter study comprising of variations in initial gas content, gas injection rate (via stellar mass loss processes), galaxy mass and amplitude of infall. From the simulation results we track variations in both physical quantities (e.g. gas mass) and directly observable quantities (e.g. X-ray luminosities). The luminosity of the galaxy's X-ray halo is found to compare favourably with the observationally determined correlation with optical blue band luminosity ($L_X : L_B$) relation. Factors affecting the X-ray luminosity are explored and it is found that the gas injection rate is a dominant factor in determining the integrated luminosity. Observational properties of the material stripped from the galaxy, which forms an X-ray wake, are investigated and it is found that wakes are most visible around galaxies with a substantial initial gas content, during their first passage though the cluster. We define a statistical skewness measure which may be used to determine the direction of motion of a galaxy using X-ray observations. Structures formed in these simulations are similar to the cold fronts seen in observation of cluster mergers where a sharp increase in surface brightness is accompanied by a transition to a cooler region.

Key words: galaxies: clusters: kinematics and dynamics - galaxies: interactions - intergalactic medium - X-rays: galaxies - galaxies: clusters: Virgo

1 INTRODUCTION

Most galaxies are not isolated but reside in clusters or groups of galaxies (Tully 1987) where a number of mechanisms may affect the nature and evolution of the galaxy. These mechanisms include tidal interactions, galaxy harassment, and ram pressure stripping. Ram pressure stripping, which is the subject of this paper, has been identified in X-ray observations of several nearby elliptical galaxies e.g. M86 (Rangarajan et al. 1995, White et al. 1991, Forman et al. 1979) and NGC 4472 (Irwin & Sarazin 1996) in the Virgo Cluster and NGC 1404 in the Fornax cluster (Paolillo et al. 2002). In these relatively nearby cases it is possible to directly image the X-ray emission surrounding the galaxy, which is distorted into an X-ray wake by the stripping process. Spectral analysis can yield information on the temperature and metallicity structure lending further weight to the hypothesis that the wake is the result of a stripping process rather than an accretion process (Rangarajan et al. 1995).

To detect the effects of ram pressure stripping in more distant galaxies requires a different approach. As wakes are often low surface brightness features it is difficult to image

wakes in distant systems, particularly when viewed against a bright cluster background. If stripping affects global properties, such as the total X-ray luminosity of the galaxy, this could be detected, for example in an environmental dependence of the L_B relation. It is currently unclear how a galaxy's X-ray luminosity L_X is affected by the cluster environment and, if so, whether ram pressure is a significant or dominant mechanism. Different studies of elliptical galaxies in clusters do not always draw the same conclusions (e.g. O'Sullivan et al. 2001; Brown & Bregman 2000). It is possible that the nearby wake candidates are atypical and that ram pressure stripping is not a common process. Alternatively, it may be the case that L_X suppression is not a good indicator of the presence of stripping or that other processes affect L_X more than ram pressure.

Numerical simulations of stripping processes provide valuable insights into physical processes and their observable consequences which cannot be obtained from analytical models alone. Previous work in this area includes simulations of elliptical galaxies moving through a uniform cluster environment at a constant velocity which is appropriate for galaxies on a circular orbit within a cluster (e.g. Gaetz et al.

1987; Balsara et al. 1994). Given the constant ram pressure in these cases a quasi-steady state is reached and certain scaling relations (e.g. for retained gas mass fraction) may be derived (Gaetz et al. 1987). Although Kent & Gunn (1982) determine that galaxy orbits in the Coma cluster cannot be primarily radial, the case of a radial, or highly elliptical orbit, is still of considerable interest in representing accretion of material from the field or a sub-cluster merger. NGC 4839 is the dominant galaxy in a sub-cluster which is falling into the Coma cluster and XMM-Newton observations (Neumann et al. 2002, Neumann et al. 2001) show an X-ray tail around NGC 4839 which is interpreted as a wake of stripped material. As clusters grow via minor mergers there may be many such cases of large elliptical galaxies passing through clusters on radial paths. Takeda et al. (1984) simulate radial infall for a large ($10^{12} M_{\odot}$) elliptical galaxy tracking the galactic gas evolution for number of cluster crossings, finding a periodic variation in gas content after the first cluster passage. A detailed study of elliptical galaxies on elliptical orbits has been carried out by Toniazzo & Schindler (2001) using 3-dimensional simulations yielding detailed information on the gas dynamic processes and variations in X-ray luminosity. A broad parameter study of stripping from dwarf galaxies has been carried out by Mori & Burkert (2000) for galaxy masses in the range 10^6 – $10^{10} M_{\odot}$. Interactions between dwarf galaxies and the cluster environment affect the chemical evolution of galaxies and clusters; higher metallicity gas which is stripped from the galaxy will enrich the lower metallicity medium of the cluster, and the depletion of the gas content may prevent further star formation. Ram pressure stripping may also influence the morphology density relation (Dressler 1980).

Our aim in the present study is to use 2-D hydrodynamic simulations of a spherical galaxy falling radially into a cluster in order to determine the effect of such an event on the galaxy and the impact on observable properties such as the galaxy's X-ray luminosity. A number of parameter variations are investigated enabling determination of the sensitivity of the results to the value of a given model parameter. This parameter study indicates not only how sensitive our results are to the choice of model, but also what are the consequences of genuine variations in the physical parameters of a galaxy population. The aim of the parameter study presented here is to focus on high mass galaxies where interactions with the intra-cluster medium lead to more directly observable consequences than in the lower mass cases considered by Mori & Burkert (2000). X-ray observations of galaxy wakes caused by stripped material could be used to elucidate the full 3-D nature of galaxy dynamics (Merrifield 1998) but a sample of wakes observed in a given cluster will not be unbiased hence it is important to understand the factors which influence which galaxies will host observable wakes.

Section 2 presents the details of the galaxy model, the model cluster into which the galaxy falls and the numerical scheme used. Section 3 consists of a number of subsections which present the results from the simulation parameter study. Subsection 3.1 gives an overview of the stripping phases which occur during a cluster crossing, subsection 3.2 examines the variations of the galactic gas content, the observable consequences of which are dealt with in subsection 3.3. Subsection 3.4 examines the properties of the

wake of stripped material and subsection 3.5 explores the properties of the bow shock. The effect of placing the model galaxy in the harsher stripping environment of a hotter cluster is examined in section 4. Finally, section 5 presents a discussion of the results and conclusions which may be drawn.

2 OVERVIEW OF THE MODEL

This section presents details of the canonical, or typical, simulation run. The parameter study involves varying each parameter from its value in the canonical model in order to determine the effect of altering a single model component. For example, to investigate the effect of increasing the size of the pre-existing gas halo, the initial extent of the halo was doubled whilst all other parameters retained their standard values. When changing the mass of the model galaxy, more than one simulation parameter was altered. The mass of the dark matter halo was changed and other parameters calculated so as to be consistent with the increased dark matter mass as described below.

2.1 The galaxy model

The model galaxy consists of two distinct components; a stellar component and a dark matter component. The dark matter component is considered to be the more massive and hence dominates the gravitational influence of the galaxy, however the stellar component is significant not only due to its gravitational effects but also due to sources of gas injection which come from stellar mass loss processes (e.g. type Ia supernovae, planetary nebulae and stellar winds). These injection processes place additional gas onto the grid within the galaxy and can replenish a stripped gas halo. A model galaxy is constructed by specifying a mass for the dark matter halo and then using a number of scaling relations to determine values for subsequent parameters.

2.1.1 Dark matter component

Numerical simulations of structure formation by Navarro et al. (1997) indicate that dark matter haloes have a universal cuspy density profile where the dark matter density at a distance r from the centre of the halo is given by

$$\rho_{\text{dm}}(r) = \frac{\rho_0}{cx(1+cx)^2} \quad (1)$$

where

$$x = \frac{r}{r_{200}}, \quad (2)$$

c is the concentration parameter which governs the degree of central concentration of the halo. In hierarchical models of structure formation smaller objects form earlier in the evolution of the universe and hence are more centrally concentrated so the concentration parameter scales with halo mass. The scaling relation used was that determined from the simulations of Bullock et al. (2001),

$$c = 10 \left(\frac{M_{\text{halo}}}{2.1 \times 10^{13} M_{\odot}} \right)^{-0.14}. \quad (3)$$

The value of r_{200} depends on the redshift of formation of the object and the matter density of the Universe at that redshift which in turn depends on the assumed cosmology. Due to the difficulties in determining these quantities a typical value of $r_{200} = 50$ kpc was chosen for $M_{\text{halo}} = 2.0 \times 10^{12} M_{\odot}$ and it was assumed that $r_{200} \propto M_{\text{halo}}^{1/3}$. The final constraint imposed on the dark matter halo is that the dark matter distribution is truncated at r_{200} , so that

$$M_{\text{halo}} = \int_0^{r_{200}} \rho_{\text{dm}}(r) 4\pi r^2 dr. \quad (4)$$

2.1.2 Stellar component

Given the properties of the dark matter halo it is possible to define a stellar population which is consistent with the observed properties of elliptical galaxies. The total blue band luminosity of the stellar population was determined assuming a total mass to light ratio of $50 M_{\odot}/L_{\odot}$ based on Table 1 from Finoguenov & Jones (2000) (N.B. this is the mass to light ratio for the whole galaxy, values measured using an aperture smaller than r_{200} will measure smaller mass to light ratios as dark matter dominates at large radii). For the old stellar population of an elliptical galaxy the mass to light ratio of the stars themselves will be greater than unity. The value adopted was

$$\frac{M_*}{L_*} = 13 \frac{M_{\odot}}{L_{\odot}} \quad (5)$$

based on an average value from the sample of Finoguenov & Jones (2000) where the original mass to light ratios were determined by Lauer (1985). Given these assumed mass to light ratios the total stellar mass may then be determined. Two mass to light ratios are required as the first dictates the amount of dark matter relative to the galaxy's blue band luminosity and the second describes the mass to light ratio of the stars only which depends on the age of the stellar population. The stars are assumed to be distributed according to a King-type distribution as used by Balsara et al. (1994) i.e.

$$\rho_*(r) = \frac{\rho_*(0)}{1 + (r/R_c)^2} \quad (6)$$

where R_c is the core radius (2.5 kpc) and the stellar distribution is truncated at $R_H = 20$ kpc. The central stellar density $\rho_*(0)$ is determined using

$$M_* = \int_0^{R_H} \rho_*(r) 4\pi r^2 dr. \quad (7)$$

2.1.3 Gas halo

The pre-existing gas halo, which surrounds the galaxy at the start of the simulation, is assumed to extend out to r_{200} and be composed of material of solar metallicity (Matsushita et al. 2000). The halo is initially isothermal at a temperature of 0.8 keV, the measured temperature of the gas halo surrounding M86 (Matsushita et al. 2000) which is of a similar mass to our model galaxy. The effects of radiative cooling are included which causes the dense central regions to cool appreciably from the initial temperature. The initial conditions are such that the halo is in hydrostatic equilibrium with the galaxy potential and that there is pressure

continuity between the outer edge of the halo and the surrounding intra-cluster medium (ICM).

2.1.4 Mass replenishment and drop out

Stellar mass loss processes (e.g. type Ia supernova (SNIa), planetary nebulae) will inject matter and energy into the galaxy which affects the X-ray halo. The distribution of replenished material is assumed to follow the stellar distribution so that the mass injection rate as a function of radius is

$$\dot{\rho}_{\text{rep}} = \alpha_* \frac{\rho_*(0)}{1 + (r/R_c)^2} \quad (8)$$

where $\alpha_* = 5.4 \times 10^{-20} \text{ s}^{-1}$ is the specific mass loss rate for an old stellar population as determined by Brighenti & Mathews (1998).

The energy injection is dominated by SNIa and a component due to the velocity dispersion of the stars in the galaxy potential. A supernova rate typical of an elliptical galaxy is 0.1 SNU (Finoguenov & Jones 2000; Cappellaro et al. 1993) (1 SNU = 1 supernova per year per $L_{B\odot}$) and the typical energy injection from one SNIa is 8×10^{50} ergs.

The velocity dispersion of the galaxy was estimated using the Faber-Jackson relation

$$\frac{L_V}{2 \times 10^{10} L_{\odot}} = \left(\frac{\sigma}{200 \text{ km s}^{-1}} \right)^4 \quad (9)$$

(Faber & Jackson 1976) where L_V was determined from the blue band luminosity L_B assuming a $(B - V)$ colour of 0.95 (Bender et al. 1993).

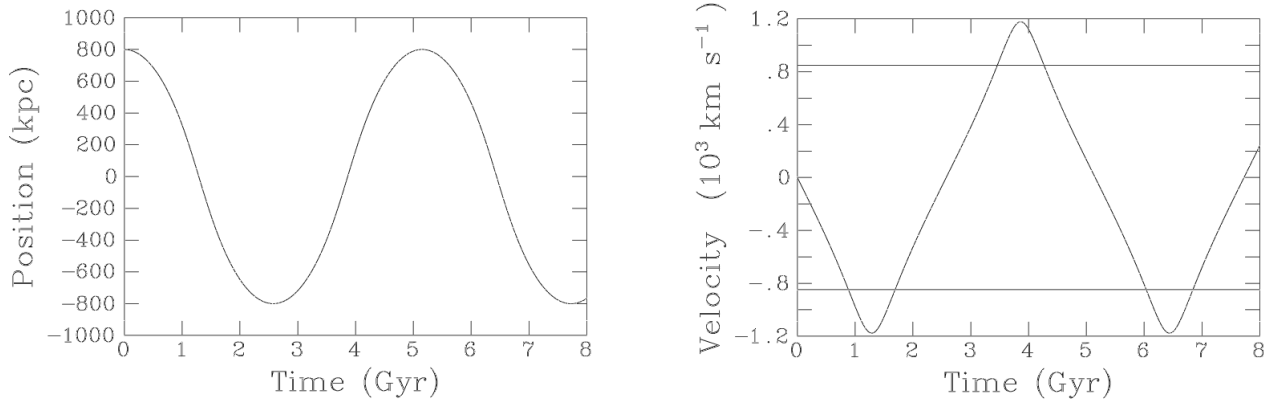
In addition to processes which act as sources of gas there are other processes which act as sinks to remove gas (e.g. star formation or accretion onto a central compact object). Radiative cooling is included, using a Raymond-Smith thermal plasma model with solar metallicity, which results in cool dense gas accumulating at the centre of the galaxy where it is allowed to drop out of the flow and is removed over a given time-scale. In a cell where the gas density is above the critical value of $\rho_{\text{do}} = 2.4 \times 10^{-24} \text{ g cm}^{-3}$ and the gas temperature is below the critical value of $T_{\text{do}} = 2 \times 10^4 \text{ K}$ gas will be removed at a rate of

$$\rho_{\text{do}} = \frac{\rho}{\tau_{\text{do}}} \quad (10)$$

where $\tau_{\text{do}} = 3 \times 10^7 \text{ yr}$. The drop out prescription used here is identical to that of Stevens et al. (1999).

2.2 Cluster model and galaxy dynamics

The model cluster was chosen to be a favourable environment for observing wakes. In order for a significant number of wakes to be observed it is required that the density of the ICM be high enough that ram pressure is sufficient to distort the galaxy halo, but not so high that the background emission from the cluster obliterates the signature of the wake. The optimum range of cluster temperatures to fulfil these criteria is 2–3 keV (Stevens et al. 1999). The parameters of the cluster model were based on observations of the cluster Abell 160, a dynamically relaxed cluster at a temperature of 2.7 keV and a distance of 270 Mpc, in which a statistical



(a) Time variation of galaxy position relative to the cluster centre. Positive values indicate that the galaxy is located to the right of the cluster centre and negative values indicate that the galaxy is located to the left.

(b) Time variation of galaxy velocity. Horizontal lines mark the cluster sound speed of 847 km s^{-1}

Figure 1. Galaxy dynamics.

detection of a number of wakes has been found (Drake et al. 2000).

The dynamics of the galaxy were modelled by free-fall in the cluster potential, neglecting dissipation processes such as dynamical friction but including the effect of tidal forces. The form of the cluster potential was chosen to be the same as that used by Toniazzo & Schindler (2001)

$$\phi(r) = \sigma_c^2 \ln \left[1 + \left(\frac{r}{r_c} \right)^2 \right] \quad (11)$$

where σ_c is the cluster velocity dispersion and r_c is the cluster core radius. The free fall frame of reference in which the simulation is conducted transforms away first order gravitational effects but not tidal effects. For a potential of this form, tidal forces are greatest at the cluster core radius. A core radius of 400 kpc was adopted to match the value of White et al. (1997) for Abell 160. The galaxy was allowed to fall into the cluster, on a radial trajectory, from an initial position of 2 cluster core radii from the centre and an initial state of rest, resulting in the dynamics shown in Fig. 1. The shape of the cluster potential is fixed by eqn. 11 but the depth of the potential, parameterized by the cluster velocity dispersion, is not fixed. The X-ray surface brightness $S(w)$ at a projected distance w from the centre of a relaxed cluster is found to be well fitted by a beta model with $\beta = 2/3$

$$S(w) = \frac{S_0}{[1 + (w/r_c)^2]^{3/2}} \quad (12)$$

which results from a gas density profile of the form

$$\rho = \frac{\rho_0}{1 + (r/r_c)^2} \quad (13)$$

Gas in hydrostatic equilibrium in the potential given in eqn. 11 will have the density distribution given in eqn. 13 if

$$\sigma_c^2 = \frac{kT}{\mu m_H} \quad (14)$$

where μm_H is the mean mass per ICM particle. A value of $\sigma_c = 656 \text{ km s}^{-1}$ was used, derived from eqn. 14 with a temperature of 2.7 keV. The central ICM number density was determined by relating the total X-ray luminosity L_X and the central surface brightness S_0 for the surface brightness profile given in eqn. 12

$$L_X = 8\pi^2 S_0 r_c^2. \quad (15)$$

The central surface brightness may be related to the central emissivity and hence to central number density. Assuming a plasma composed of hydrogen and helium in the ratio 10:1 the total central number density was estimated to be $6.17 \times 10^{-4} \text{ cm}^{-3}$ for $L_X = 2.7 \times 10^{43} \text{ erg s}^{-1}$ (White et al. 1997).

2.3 Numerical scheme

The numerical scheme chosen for this application was the VH-1 implementation of the Piecewise-Parabolic Method (Colella & Woodward 1984) which offers good resolution of shocks in complex flows and has been extensively used in a variety of astrophysical contexts (Blondin et al. 1990, Richards & Ratliff 1998 and Strickland & Stevens 2000). The numerical grid was a uniform Cartesian grid of 800×400 cells with a size of $x = 1.6 \times 10^{24} \text{ cm}$, $y = 8.0 \times 10^{24} \text{ cm}$ where the centre of the galaxy was located at $x = 8.0 \times 10^{24}$, $y = 0$. In an axi-symmetric case, such as this, it is only necessary to simulate the top half of the galaxy and the symmetry of the situation can be used to reflect the flow field in the x -axis to obtain the full flow field which results in a significant saving in computation time. The size of the grid as a whole was chosen such that features of interest, such as tails of stripped material and shocks, should not propagate off the grid. As the galaxy moves both from right to left and from left to right during the course of the simulation it is necessary to centre the galaxy with respect to the x -axis.

The cells subtend an angle of ~ 0.5 arcsec at a distance of 270 Mpc (the distance of Abell 160) which matches the spatial resolution of the Chandra X-ray observatory, currently the best available X-ray spatial resolution.

Boundary conditions at the left and right of the grid were fixed inflow or fixed outflow conditions to account for the movement of the simulation frame in the gravitational potential of the model cluster (e.g. fixed inflow at the left boundary and fixed outflow at the right boundary for a galaxy moving from right to left). The magnitude of the inflow velocity at one boundary was equal to the magnitude of the outflow velocity at the other boundary so that the direction of motion could be reversed in a consistent fashion. The fixed inflow/outflow densities were different due to density gradients in the ICM. The size of the grid is not negligible compared to the size of the cluster so the ICM density is different at the left and right boundaries. To ensure a physically consistent model for the cluster, it is necessary to ensure the ICM contains a density gradient consistent with hydrostatic equilibrium in cluster potential given by eqn. 11. If eqn. 14 is obeyed then the resulting X-ray surface brightness distribution of the ICM will be given by a beta model with $\beta = 2/3$ as in eqn. 12. This density gradient must be present in the initial ICM distribution and must also be accounted for when calculating inflow and outflow densities at the left and right boundaries.

A reflective boundary condition must be applied to the $y = 0$ boundary in order for the symmetry of the problem to be correctly applied and an inflow/outflow condition was applied to the top of the grid to allow material to flow freely off the grid should it reach the upper boundary. Time steps were determined by application of the Courant-Friedrichs-Lewy (CFL) condition with a CFL number of 0.8.

The use of a 2D numerical grid results in a significantly shorter computation time than for a 3D grid, for comparable resolution, which is an important issue when performing the many runs required to cover a wide range of parameter space. The rate of stripping may depend on the formation of Kelvin-Helmholtz shear instabilities which can behave differently in 2D and 3D simulations. Brüggén & Hillebrandt (2001a) compare the mixing rate due to such instabilities in 2D and 3D simulations and find that the steady state mixing rate is very similar, supporting the validity of the 2D treatment used here. It should be noted, however, that if magnetic field effects are included there is significant disagreement between 2D and 3D simulations (Brüggén & Hillebrandt 2001b). As no magnetic fields are explicitly included in these simulations we proceed with a 2D model.

3 RESULTS

In this section results are presented from the parameter study examining both observational quantities, such as X-ray luminosity and surface brightness profiles, and other quantities (e.g. gas mass) which, whilst not directly observable, play an important role in determining the nature of the galaxy. The parameters involved in the study were: galaxy mass, mass injection rate, initial gas halo extent and the starting position of the galaxy (hence the maximum velocity reached) as shown in Table 1.

3.1 Initial cluster crossing

Density distributions from the canonical run are shown in Fig. 2 to illustrate various phases of the stripping process. Fig. 2(a) is the initial gas distribution (i.e. a spherically symmetric halo in hydrostatic support) which is beginning to be stripped in Fig. 2(b) where the motion is subsonic. The halo presents a sharp edge in the upstream direction but stripping, via Kelvin-Helmholtz instabilities, prevents a sharp delineation in other regions. Fig. 2(c) is taken from a supersonic regime and a bow shock, and associated density enhancement, can be seen. The final frame (Fig. 2(d)) is taken at the end of the first cluster crossing and density enhancements are seen in front of the galaxy. As the galaxy approaches the edge of the cluster, and the ram pressure decreases, material which was previously confined behind the galaxy moves forward causing the enhancements seen in Fig. 2(d).

3.2 Gas content

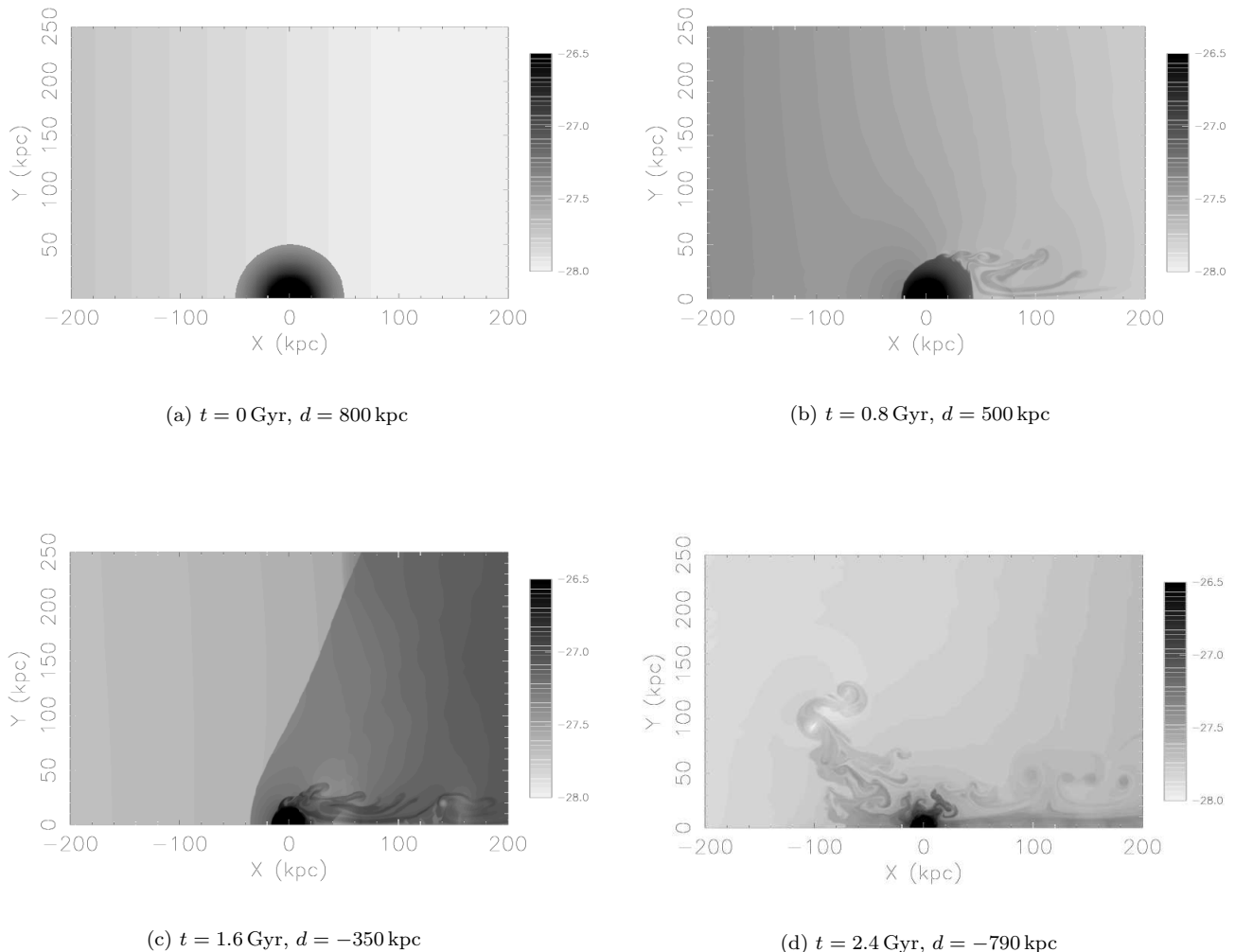
The variation in gas mass within the central 40 kpc, for galaxies with different initial halo extents, is plotted in Fig. 3(a). The vertical lines mark regions where the galaxy velocity is supersonic (indicated by Sup.) close to core passage. A more extensive gas halo is more massive not only due to its larger volume but also due to the higher central density which is necessary to satisfy the conditions of hydrostatic support and pressure continuity at the halo truncation radius. Both the canonical and extended haloes experience an initial period during which the pre-existing halo is stripped before moving into a cyclic phase where the enclosed gas mass is at a maximum at core passage. The duration of the initial stripping phase depends on the halo mass at the start of the simulation (~ 2.5 Gyr for the canonical halo and ~ 4.0 Gyr for the larger halo) but after this phase all runs behave in a very similar fashion indicating that after ~ 4 Gyr (time of second core passage) the signatures of the initial gas content are no longer present. The large enclosed mass close to core passage is somewhat surprising, but one should bear in mind that this gas is not necessarily gravitationally bound to the galaxy. Fig. 4(a) shows the mass of gas which is gravitationally bound to the galaxy for the three cases considered above. The gas in a cell where the mass density is ρ , the particle number density is n , the fluid velocity u and the temperature T is considered to be bound if

$$\frac{1}{2}\rho u^2 + \frac{3}{2}nkT + \rho\psi_G < 0 \quad (16)$$

where ψ_G is the gravitational potential of the galaxy evaluated at the cell location. In contrast to Fig. 3(a), which plots all gas within 40 kpc irrespective of whether it is bound, Fig. 4(a) indicates that the supersonic phase results in a substantial amount of the bound gas being stripped. This indicates that around the time of core passage there is a concentration of gas within 40 kpc which is not gravitationally bound to the galaxy and the question of where this gas is located is raised. Fig. 5 plots the ratio of gas density after 3.9 and 3.6 Gyr, i.e. the gas density at one of the peaks in Fig. 3(a) divided by the gas density just after the peak starts to form. This indicates that the rise in unbound gas mass within 40 kpc is associated with an enhancement of

Table 1. Details of runs forming the parameter study

Parameter	Low Value	Standard Value	High value
Halo extent	25 kpc	50kpc	100 kpc
Mass replenishment rate	$0.12 M_{\odot} \text{ yr}^{-1}$	$1.2 M_{\odot} \text{ yr}^{-1}$	$3.6 M_{\odot} \text{ yr}^{-1}$
Dark matter halo mass	$1.0 \times 10^{12} M_{\odot}$	$2.0 \times 10^{12} M_{\odot}$	$4.0 \times 10^{12} M_{\odot}$
Infall radius	400kpc	800 kpc	1600 kpc

**Figure 2.** Gas density distribution from the initial infall of the canonical run. The time (t) quoted is that since the start of the simulation and d is the distance from the cluster centre which is positive when the galaxy is to the right of the cluster centre and negative when to the left. The logarithmic greyscale shows the gas density in units of g cm^{-3} .

material behind the shock front. When the halo extent is reduced by half, the initial period of stripping prior to the cyclic behaviour is not seen as the initial gas content does not exceed that present during the latter phases as in the other cases.

The gas mass for runs with different mass replenishment rates is shown in Fig. 3(b). In the previous series of runs the initial gas content was different but the injection

rate was constant resulting in the evolution of the gas content in the model galaxies converging. In this second case the initial gas content is constant but the injection rate varies, resulting in a gas content which displays an initial period of divergence. At later times (after $\sim 3 \text{ Gyr}$) the gas content again behaves in a cyclic manner but with a base level which depends on replenishment rate. The rate at which the mass increases prior to the supersonic phase is a function of the

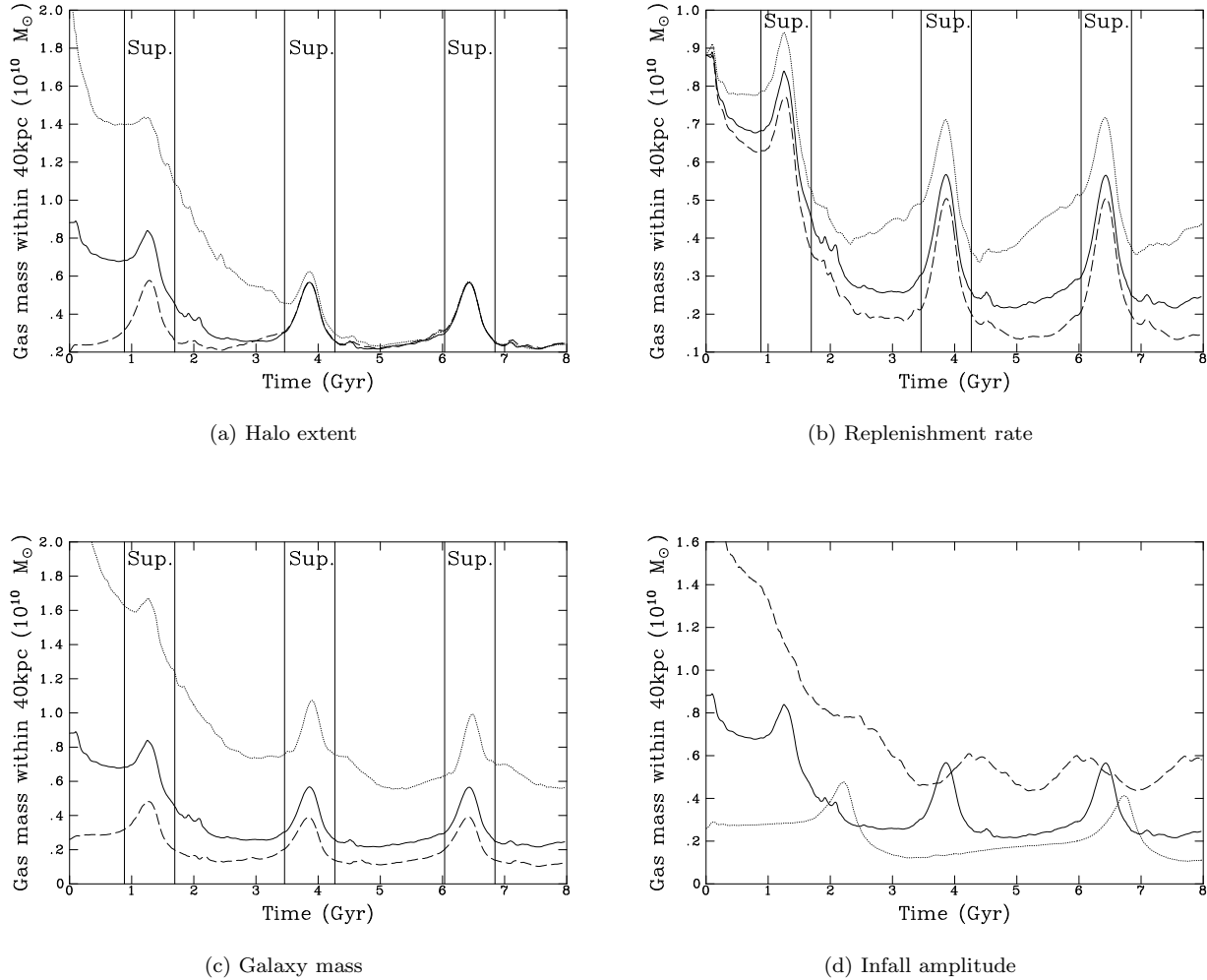


Figure 3. Time variation of the gas mass within 40 kpc of the galactic centre. In each case the canonical run is plotted as a solid line, the dashed line represents a reduction in the parameter and the dotted line an increase in the value of the parameter. Time periods where the galaxy velocity is supersonic are marked “Sup.”. Periods of supersonic velocity are not shown in Fig. 3(d) as they are different for each case.

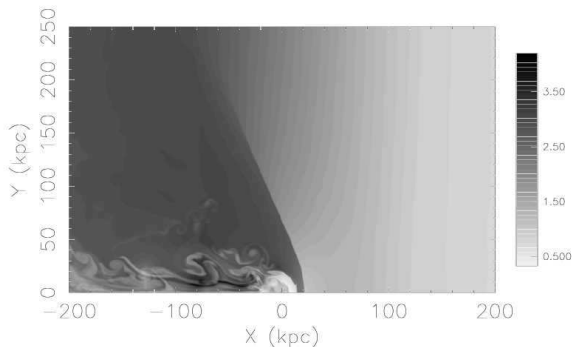


Figure 5. Gas density field after 3.9 Gyr divided by gas density field after 3.6 Gyr showing the location of the density enhancement around the time of core passage. The galaxy is moving from left to right at both times.

mass replenishment rate with higher injection rates resulting in more rapid rises in gas content. The higher injection rate run shows how in subsonic phases there is an accumulation of gas, during the supersonic phase the gas content is high due to the accumulation of unbound gas, and after the supersonic phase much of the gas associated with the galaxy has been depleted and is replenished during the next subsonic phase. The bound gas content (Fig. 4(b)) better shows the effect of alternate cycles of net gas accumulation during subsonic phases and net stripping during supersonic and some subsonic regimes. When the mass injection rate is at its lowest it is seen that the net stripping phase starts sooner than in other runs. During subsonic motion, stripping does occur from the outer edge of the halo but the net gas budget is a combination of the stripping and drop out loss mechanisms, and the mass injection replenishment mechanism. Whether there is net loss or gain of gas during

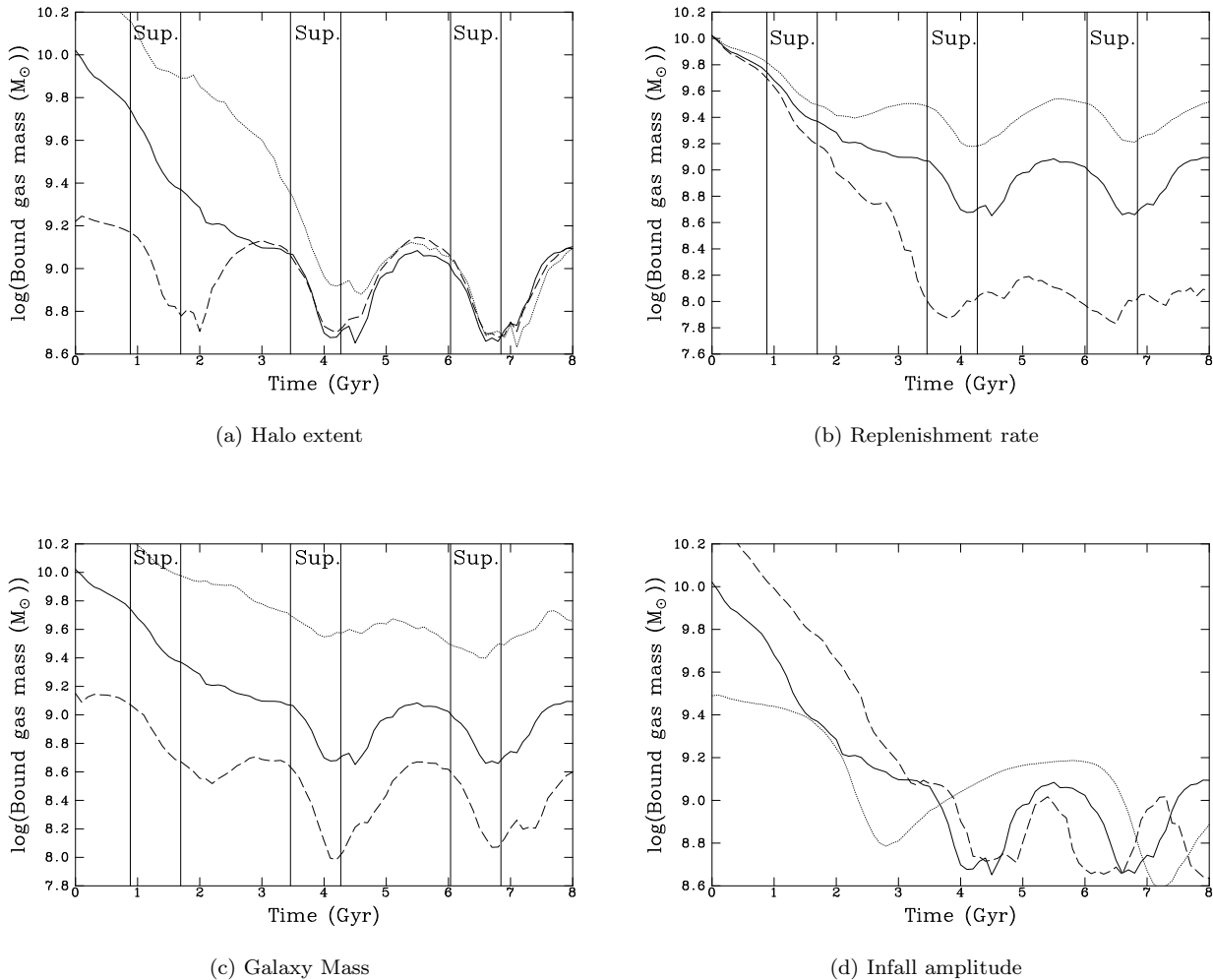


Figure 4. Total gas mass which is gravitationally bound to the galaxy (c.f. Fig. 3 which plots all gas within a fixed 40 kpc radius). In each case the canonical run is plotted as a solid line, the dashed line represents a reduction in the parameter and the dotted line an increase in the value of the parameter.

a subsonic phase will depend largely on the effectiveness of subsonic stripping compared to the mass injection rate.

The next series of runs involves variation of the galaxy mass which is achieved by changing the dark matter halo mass and assuming length scales vary as $r \propto M^{1/3}$. By varying the total galaxy mass, not only is the depth of the potential well increased but also the mass replenishment rate (which is proportional to the stellar mass), the mass replenishment temperature (which depends on the stellar velocity dispersion) and the extent of the initial halo (which is subject to the same linear scaling factor as the other galaxy length scales). The resulting interdependency of parameters means that more care is required in interpreting the results of these particular simulation runs but gives a self consistent galaxy model. The gas mass fraction, within a 40 kpc radius, for each galaxy is plotted in Fig. 6 where the gas mass fraction has been calculated by dividing the gas mass within 40 kpc by the total galaxy mass (dark matter and stellar components). The gas mass fraction indicates that the more massive galaxies have a higher gas content in the subsonic

regime. The enhancement due to the bow shock, during supersonic phases, is greater for less massive galaxies. As the concentration parameter scales inversely with galaxy mass, the less massive galaxies will be more centrally concentrated and this may result in a more prominent shock. The bound gas content (Fig. 4(c)) indicates that more massive galaxies not only have more gravitationally bound gas but also the variation in this gas content is less. The deeper gravitational potential wells of the more massive systems would be expected to make depletion of gas by ram pressure stripping less effective.

The final parameter to be varied is the initial starting position from which the galaxy falls into the cluster. This affects the galaxy dynamics (i.e. the maximum speed reached by the galaxy and also the time taken to cross the cluster, hence the periodicity in mass variation). When the infall radius is reduced to 400 kpc the maximum velocity reached is 770 km s^{-1} and the crossing time is $\sim 1.7 \text{ Gyr}$; in this case the galaxy velocity never becomes supersonic. An increased infall radius of 1600 kpc raises the maximum velocity to

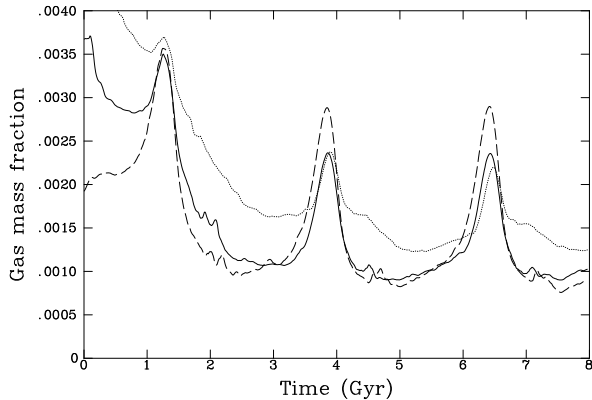


Figure 6. Gas mass fraction within 40 kpc of the galactic centre for galaxies with differing masses (solid: canonical, dashed: less massive, dotted: more massive). This is essentially Fig. 3 with the y -axis divided by the total mass of the galaxy.

1560 km s^{-1} with a crossing time of ~ 4.5 Gyr. The initial state of the gas halo also varies in these runs. When the starting position of the galaxy is closer to the cluster core, where the ICM density is higher, the halo density must also be higher to maintain pressure continuity at the halo boundary and hydrostatic support. The time variation of the gas mass for these runs, shown in Fig. 3(d), clearly indicates the different dynamical time-scales: with a larger infall the peaks at core passage are ~ 4.5 Gyr apart, with a smaller infall the peaks in mass are separated by ~ 1.7 Gyr. With a larger infall there is a marked difference in gas mass before and after the peak at core passage suggesting that substantial stripping occurs during the supersonic phase but that this is masked by the density enhancement from the unbound gas. The gas mass variation, with the time axis scaled to the cluster crossing time (Fig. 7), shows that the variations in gas mass occur at similar points during the dynamic cycle. The bound gas variations for the above series of runs are plotted in Fig. 4(d). The canonical and smaller infall cases have a similar minimum gas content but with a smaller infall amplitude the excursions in gas content are smaller.

Analytic fits to simulation results have been derived by Gaetz et al. (1987) to determine the fraction of replenished gas which is retained in a quasi-steady state, but it should be noted that the stripping occurring in these simulations operates in a different regime. The results of Gaetz et al. (1987) are applicable during supersonic regimes only (Mach. numbers greater than unity), which applies only briefly in these simulations, and in cases where the escape velocity from the galaxy (measured at the half mass replenishment radius) exceeds the velocity of the galaxy through the ICM. In the cases considered here, for the canonical dynamics, the escape velocity is comparable with the maximum galaxy velocity hence the fitting formulae of Gaetz et al. (1987) do not, and would not be expected to, give a good fit to our results.

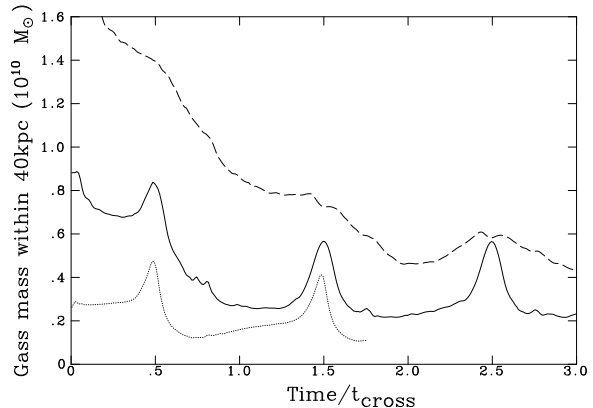


Figure 7. Time variation of the gas mass within 40 kpc of the galactic centre for galaxies falling into the cluster from different starting positions with the time axis scaled to the cluster crossing time (solid: canonical, dashed: infall from closer to the cluster centre, dotted: infall from further out from cluster centre).

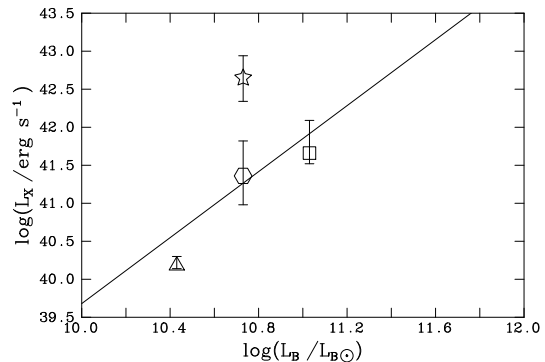


Figure 9. $L_X:L_B$ relation for four of the simulated galaxies (less massive (triangle), more massive (square), canonical mass with lower mass replenishment rate (hexagon) and canonical mass with higher mass replenishment rate (star)). L_X is the X-ray luminosity in the 0.5–2.0 keV band and L_B is the blue band optical luminosity in solar units. The solid line is the observationally determined relation of O'Sullivan et al. (2001). Bars in the L_X direction show the range in L_X during the simulation (see text for details).

3.3 Observable halo properties

The time variation of X-ray luminosity within a radius of 40 kpc, in the 0.3–8.0 keV band (i.e. a broad band Chandra or XMM luminosity), for runs with varying initial halo extents is shown in Fig. 8(a). These luminosities only include the contribution from the gas halo and no point source contribution. The total X-ray luminosity is seen to broadly follow the variations in gas mass within this fixed aperture, i.e. peaks at core passage and converges to a common pattern of fluctuations when the halo has been stripped.

The time variation of the galaxy X-ray luminosity for different values of the mass replenishment rate is shown in Fig. 8(b). The mass replenishment rate has a large impact on the X-ray luminosity; the canonical and higher mass re-

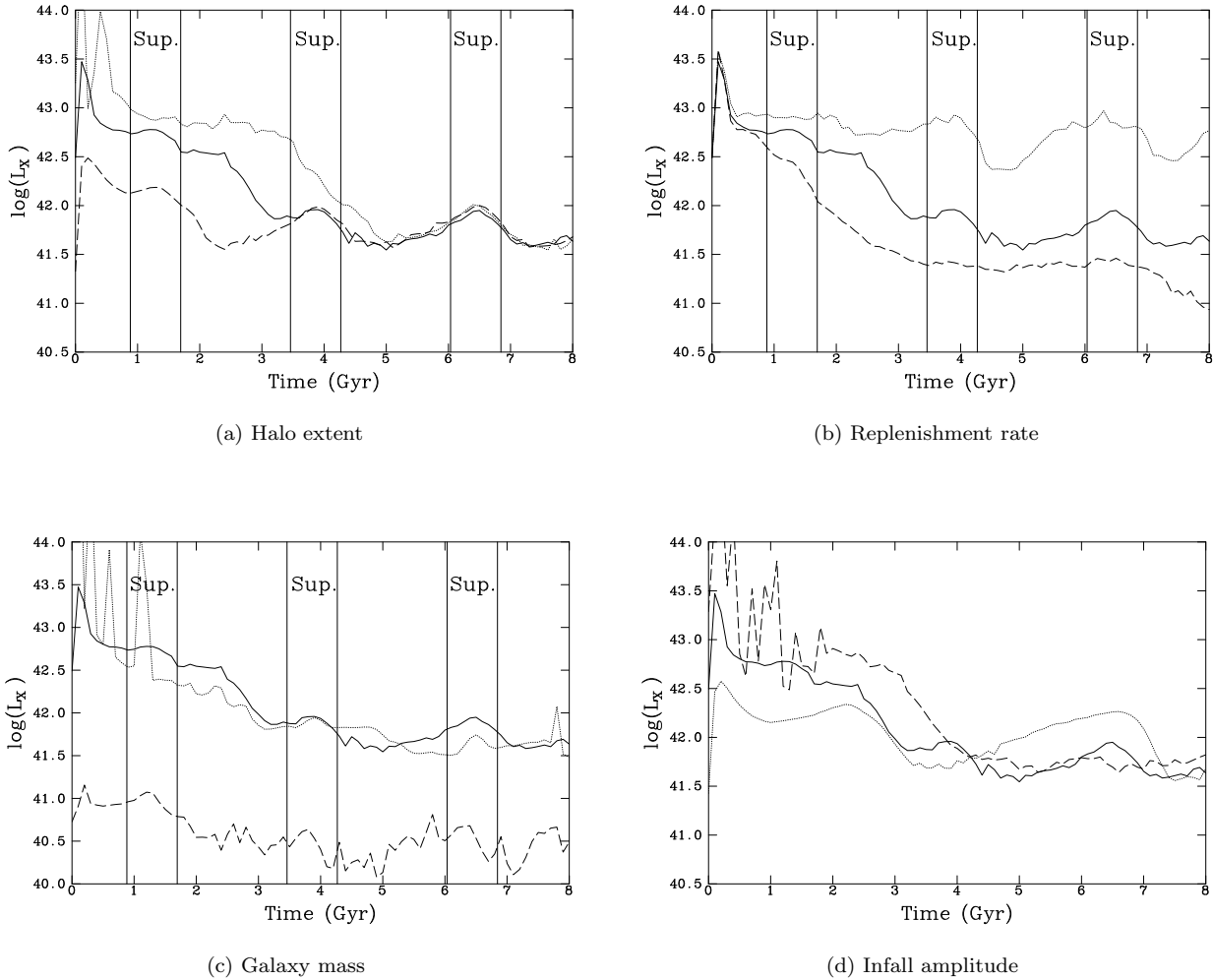


Figure 8. Time evolution of X-ray luminosity (L_X) in the 0.3–8.0 keV band for each parameter variation. In each case the canonical run is plotted as a solid line, the dashed line represents a reduction in the parameter and the dotted line an increase in the value of the parameter.

plenishment rate runs differ only by a factor of 3 in mass replenishment rate but have very different X-ray luminosities.

The time variation of the galaxy X-ray luminosity, for different galaxy masses, is shown in Fig. 8(c). The least massive galaxy has a significantly lower X-ray luminosity than the canonical case whereas, in contrast, the most massive galaxy has a similar luminosity to the canonical galaxy. The X-ray luminosity is largely governed by the central regions of the gas halo so differences in gas mass may be present which do not manifest themselves as significantly different X-ray luminosities.

The time variation of galaxy X-ray luminosity, for different infall radii, is shown in Fig. 8(d). The different cluster crossing times result in different periodicities in the L_X variations but it is not possible to distinguish between the different dynamical states based on the value of L_X alone. An $L_X:L_B$ relation for four of the simulated galaxies (lower galaxy mass, higher galaxy mass, canonical mass with lower mass replenishment rate, canonical mass with higher

mass replenishment rate) is presented in Fig. 9. The upper and lower bounds indicate the maximum and minimum L_X reached during simulation times between 2 and 8 Gyr (to avoid any initial transient effects) and the symbols indicate the mean L_X measured during the same period. The lower mass replenishment rate run is responsible for the lowest L_X for a galaxy of canonical mass, and the higher mass replenishment rate run is responsible for the highest L_X hence the inclusion of these two points indicates the range of L_X which is induced by parameter variations. The X-ray luminosities between 2 and 8 Gyr have been converted from a broad band (0.3–8.0 keV) to a soft band (0.5–2.0 keV) to enable a direct comparison between X-ray luminosities determined from ROSAT and the theoretical values derived here. A point source contribution, which scales with L_B , has been added assuming

$$\log\left(\frac{L_{ps}}{L_B}\right) = 29.45 \quad (17)$$

where L_{ps} is the contribution from point sources only

(Ciotti et al. 1991; O’Sullivan et al. 2001). The X-ray luminosities derived for these simulated systems are in agreement with the observational relation of O’Sullivan et al. (2001) which is plotted as a solid line in Fig. 9. Variations in L_X due to observing a given model galaxy at varying points in the dynamical cycle are smaller than those variations induced by differing model parameters. The largest variation for an individual model is for the model with a larger initial halo extent which experiences L_X variations of ~ 1.4 dex, however the effect of parameter variations (particularly mass replenishment rate) induces a scatter of ~ 2 dex indicating that variations in L_X are not solely due to observing galaxies at different points in the dynamical cycle but rather that there are more fundamental differences causing L_X variations.

Azimuthally averaged X-ray surface brightness profiles (0.3–8.0 keV) and temperature profiles, from various times during the first and second cluster crossings, are plotted in Fig. 10. The temperature profiles are taken directly from the simulation grid so in order for a direct comparison to be made between these profiles and observations it would be necessary to apply a deprojection analysis to the observed profiles. The surface brightness profiles consist, in general, of a central peak resulting from a cool, dense core surrounded by the cool gas associated with the galactic halo. This is embedded in the less dense, less bright, hotter ICM which results in a structure reminiscent of the cold fronts seen in cluster mergers (Vikhlinin et al. 2001a, Markevitch et al. 2000). As the profiles in Fig. 10 are azimuthally averaged, encompassing regions in front of and behind the galaxy, they lack the sharp surface brightness edges seen in Chandra observations of merging clusters. When slices along the direction of motion, in the upstream direction, are plotted they exhibit sharp temperature and surface brightness edges (see Fig. 11). The surface brightness slice (Fig. 11(a)) and the corresponding temperature slice (Fig. 11(c)) clearly indicate the presence of a cold front where a sharp decrease in surface brightness is coincident with a transition to a higher temperature region at $\log(r/\text{kpc}) \sim 1.4$. The galaxy velocity is subsonic at this time so no bow shock is present although the gas temperature does rise approaching the discontinuity as would be expected from adiabatic compression (Vikhlinin et al. 2001a, §5.3). After 1.6 Gyr the galaxy motion is supersonic and the slices (Fig. 11(b) and Fig. 11(d)) are qualitatively different to the previous subsonic case. There is still a cold front present, where a surface brightness drop coincides with a temperature rise, but at a slightly smaller radius ($\log(r/\text{kpc}) \sim 1.2$). In addition to the cold front there is also a shock front where the temperature and surface brightness both rise. The surface brightness enhancement is significantly greater across the cold front than across the shock front which is consistent with Chandra observations of Abell 3667 where both a cold front and a shock front are detected but the shock front results in a smaller surface brightness enhancement (Vikhlinin et al. 2001a). Although the size scales and temperatures in this case are different to those encountered in cluster mergers the gas dynamics are similar to a cluster minor merger. In both the case of a cluster accreting a group/smaller cluster and the case of a cluster accreting a large elliptical galaxy there is a pre-existing halo of X-ray emitting gas, confined by a dark matter halo, at a temperature below that of the ICM in the accreting system.

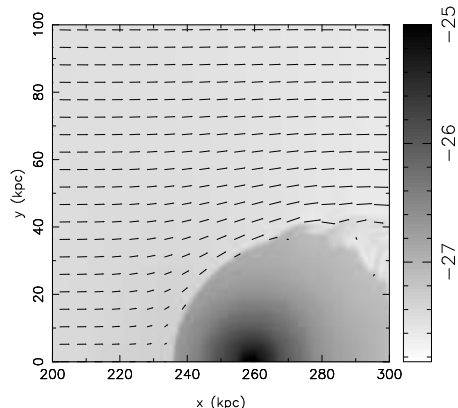


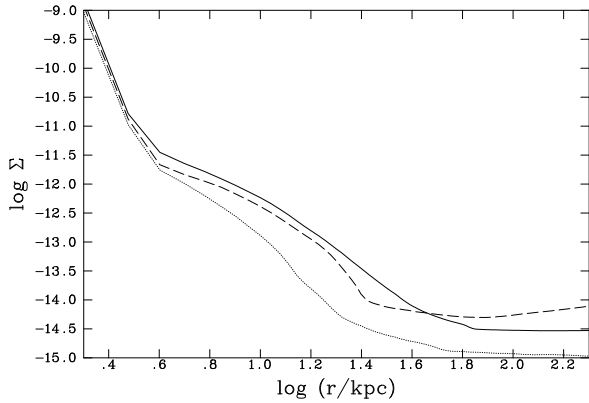
Figure 12. Density (greyscale) and velocity (vectors) around the interface between the cool and hot regions. These data are taken from the canonical run after 0.8 Gyr.

Vikhlinin et al. (2001b) show that conduction, diffusion and Kelvin-Helmholtz instabilities must be suppressed around the Abell 3667 cold front in order for the observed sharp discontinuity to be preserved. They propose that a magnetic field of order $10\mu\text{G}$ would be required in a configuration in which field lines are tangled or run parallel to the cold front. Whilst our simulations do not incorporate magnetic fields, conduction and diffusion processes will be suppressed due to the absence of these terms in the fluid equations used. Given the sharp discontinuities observed in Chandra data the non-conductive and non-diffusive fluid equations would seem to be appropriate. Vikhlinin et al. (2001b) also suggest that initially tangled magnetic fields should be stretched into a morphology where the field lines are parallel to the front due to the velocity field of the plasma around the interface between the cooler and hotter regions. The velocity field seen in our simulations (Fig. 12) clearly demonstrates this and agrees well with the flow structure in fig. 2(b) of Vikhlinin et al. (2001b).

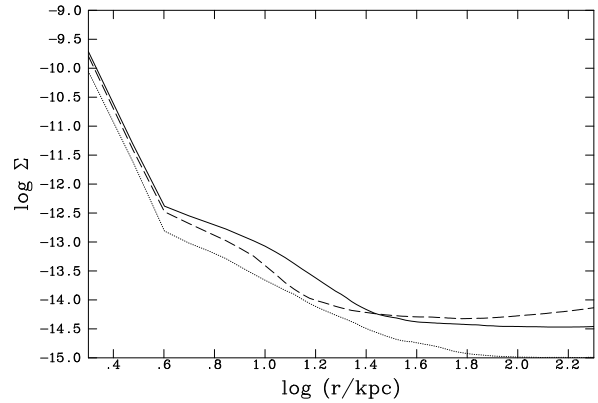
Azimuthally averaged surface brightness profiles yield useful information regarding the evolution of the gas halo. The degree of central concentration of the galaxy halo, outside the central core, may be quantified by fitting a beta model to the profile. The surface brightness at a projected distance w from the centre of the galaxy is given by

$$S(w) = \frac{S_0}{[1 + (w/r_c)^2]^{3\beta - \frac{1}{2}}} \quad (18)$$

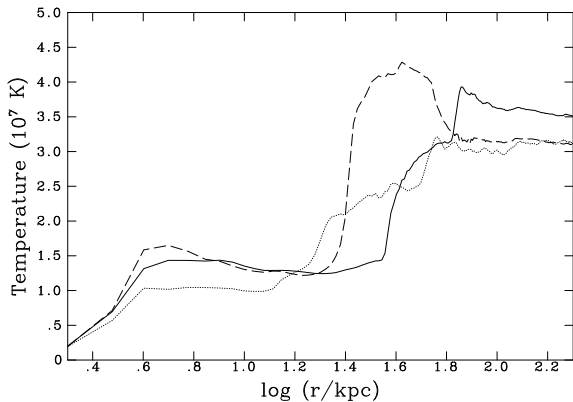
where r_c is a core radius, S_0 is the central surface brightness and the value of β parameterizes the steepness of the profile outside the core region. The time variation of the beta parameter for fits to the surface brightness distribution from all runs is plotted in Fig. 13. The model fitted to the azimuthally averaged surface brightness profile consists of three components: a beta model to fit the extended emission from the galaxy halo, a Gaussian to represent the central cool core, and a second order polynomial to account for the non-uniform cluster background. The effect of different initial halo extents (Fig. 13(a)), again shows convergence after the initial halo has been stripped. During subsonic motion stripping occurs via shear instabilities at the interface between the galaxy halo and the ICM, which is less effective than stripping in the supersonic phase. This enables replen-



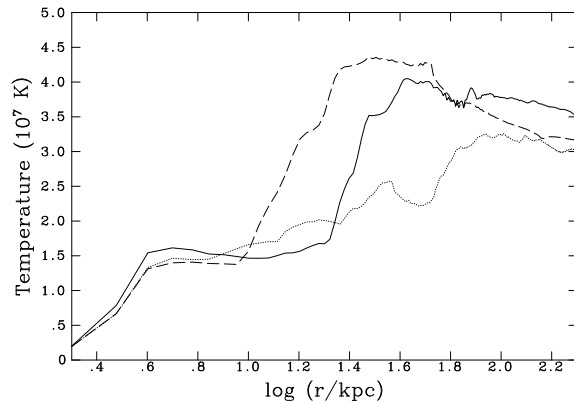
(a) Surface brightness profiles during the initial infall, after 0.8 (solid), 1.6 (dashed), 2.4 (dotted) Gyr. Surface brightness is measured in units of $\text{erg s}^{-1} \text{cm}^{-2} \text{arcmin}^{-2}$.



(b) Surface brightness profiles during the second cluster crossing, after 3.4 (solid), 4.2 (dashed), 5.0 (dotted) Gyr. Surface brightness is measured in units of $\text{erg s}^{-1} \text{cm}^{-2} \text{arcmin}^{-2}$.



(c) Temperature profiles during the initial infall, after 0.8 Gyr (solid), 1.6 Gyr (dashed), 2.4 (dotted) Gyr.



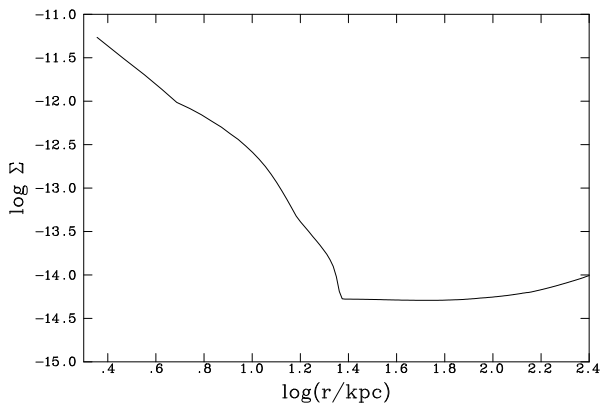
(d) Temperature profiles during second crossing, after 3.4 Gyr (solid), 4.2 Gyr (dashed), 5.0 (dotted) Gyr.

Figure 10. Azimuthally averaged radial surface brightness profiles and temperature profiles from the canonical run. The centre of the galaxy is located at $r = 0$. Surface brightness Σ is in units of $\text{erg s}^{-1} \text{cm}^{-2} \text{arcmin}^{-2}$.

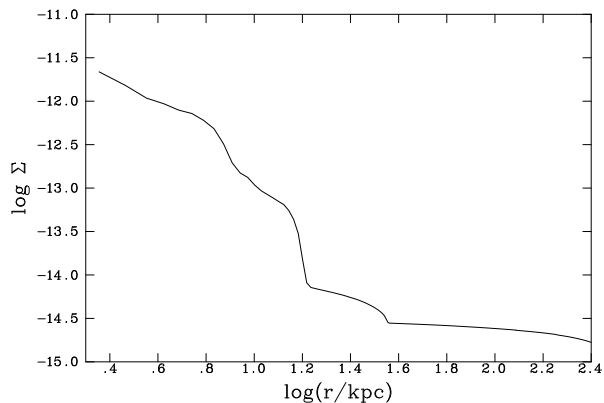
ished gas to accumulate within the galaxy. Consequently the beta value steepens as the regions of the halo where mass injection is effective ($r < R_H$) become brighter. During the supersonic phase the beta value drops as gas is stripped and the surface brightness profile becomes flatter. This effect is not always apparent during the initial crossing but can be seen clearly in the third core passage in Fig. 13(a), for example. The effect of mass injection is seen in Fig. 13(b) where higher mass injection rates lead to more rapidly rising beta values. This may be attributed to the surface brightness profile steepening more rapidly due to the increased accumulation of gas at radii $r < R_H$. When the infall amplitude is larger (Fig. 13(d)), the galaxy spends longer in the outer regions of the cluster where the ram pressure is lower, so more replenished material can accumulate and the beta value grows substantially over an extended period of time.

The diagnostic power of surface brightness profiles, rel-

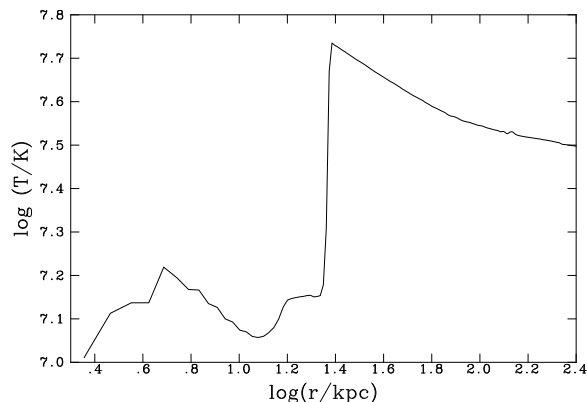
ative to integrated X-ray luminosities, is seen when comparing the runs with an increased halo mass and an increased mass replenishment rate. After 2 Gyr both simulated galaxies have a similar X-ray luminosity but, as Fig. 14 shows, there are marked differences in the surface brightness profiles. The higher mass replenishment rate, which acts only within the stellar distribution ($\log (r/\text{kpc}) < 1.3$), produces a surface brightness profile which is slightly higher in the central regions but significantly lower in the outer regions. This information regarding the spatial distribution of the X-ray emitting gas is lost when considering only integrated X-ray luminosities.



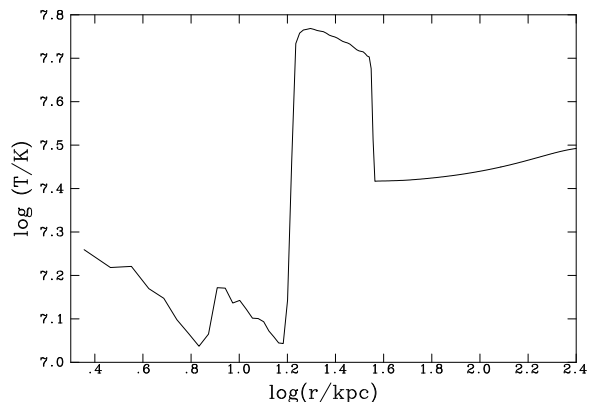
(a) Surface brightness after 0.8 Gyr in units of $\text{erg s}^{-1} \text{cm}^{-2} \text{arcmin}^{-2}$. The galaxy velocity is subsonic at this time.



(b) Surface brightness after 1.6 Gyr in units of $\text{erg s}^{-1} \text{cm}^{-2} \text{arcmin}^{-2}$. The galaxy velocity is supersonic at this time.



(c) Temperature profile after 0.8 Gyr. The galaxy velocity is subsonic at this time.



(d) Temperature profile after 1.6 Gyr. The galaxy velocity is supersonic at this time.

Figure 11. On-axis surface brightness and temperature slices from the canonical run. These slices are taken along a line parallel to the direction of the galaxy motion through the galaxy centre. The centre of the galaxy is located at $r = 0$. After 0.8 Gyr the galaxy motion is subsonic and a cold front is seen at $\log(r/\text{kpc}) \sim 1.4$, after 1.6 Gyr the galaxy motion is supersonic and a bow shock is seen at $\log(r/\text{kpc}) \sim 1.6$ in addition to a cold front at $\log(r/\text{kpc}) \sim 1.2$.

3.4 Observable wake properties

In addition to the X-ray emission from the body of the galaxy there is also emission from stripped material downstream of the galaxy which may form an observable wake. The top row of Fig. 15 shows X-ray surface brightness maps from the canonical simulation during the first, second and third crossings of the cluster at the time when the galaxy velocity is at a maximum. The highest surface brightness feature in all cases is the emission from the body of the galaxy and the next brightest is the tail of stripped material. The surface brightness of the tail is much higher during the first crossing than in subsequent crossings indicating a bias towards observing wakes around galaxies on their initial infall into a cluster. The bottom row of Fig. 15 shows surface brightness maps from the run with a larger initial gas halo. The wake formed during the first cluster crossing is brighter

and wider than that from the canonical run suggesting that the initial gas content of the galaxy has a major influence on whether wakes will be observable. X-ray luminosities, in a 0.3–8.0 keV band, for the first cluster crossing are tabulated in Table 2. These luminosities have been calculated as enhancements above the background level which would be present at the same distance from the cluster centre but away from the galaxy location. The brightness of the wake is most strongly affected by the pre-existing halo size; larger initial haloes result in more luminous wakes. The mass replenishment rate does not have a noticeable influence on wake luminosity during the first infall. Its effect only becomes apparent at later times when it affects the X-ray luminosity from the body of the galaxy.

The X-ray flux maps presented in Fig. 15 are valuable for determining which features result in the most observable

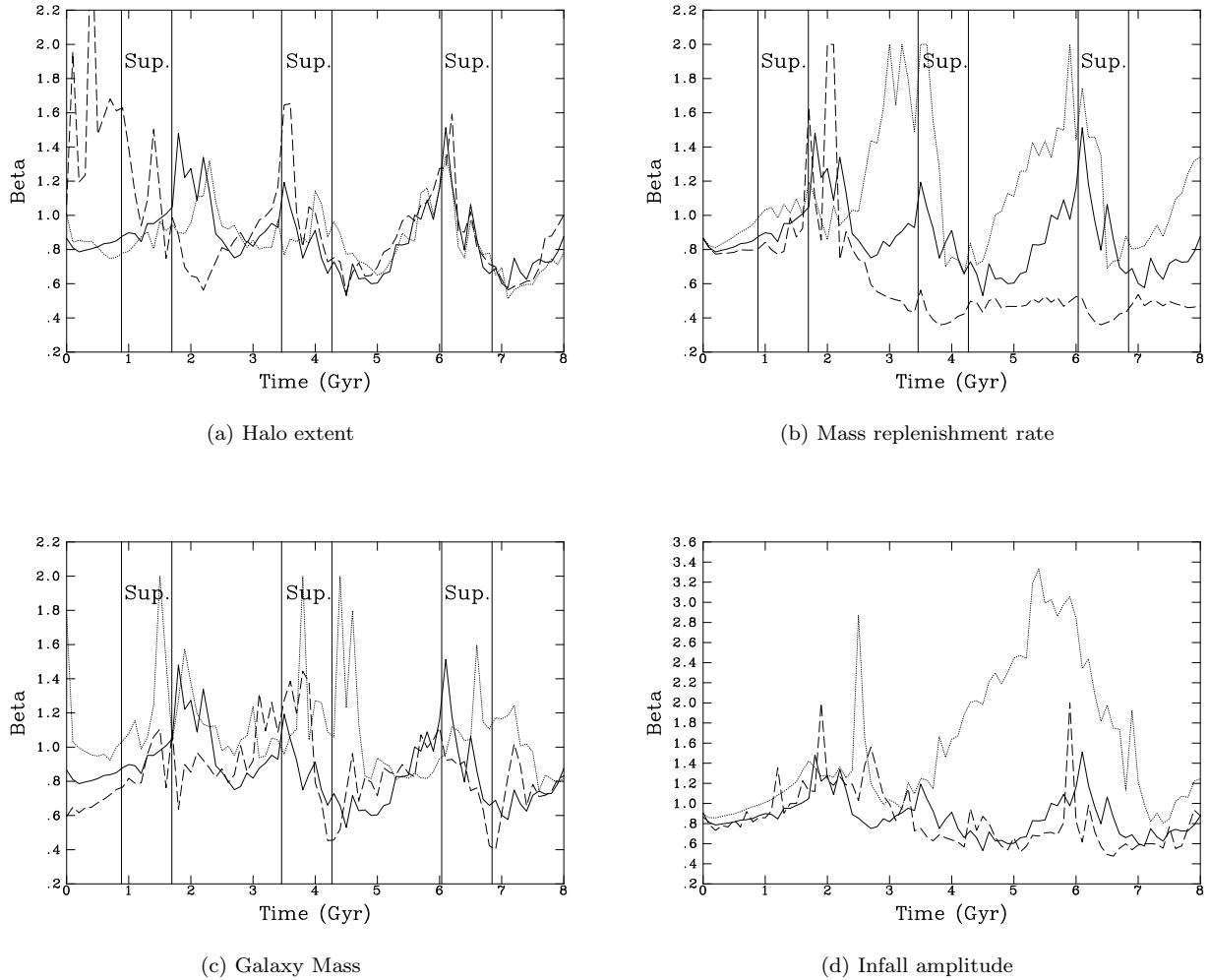


Figure 13. Time variation of beta values from fits to surface brightness profiles. Beta parameterizes the steepness of the surface brightness profile outside the central core region. In each case the canonical run is plotted as a solid line, the dashed line represents a reduction in the parameter and the dotted line an increase in the value of the parameter.

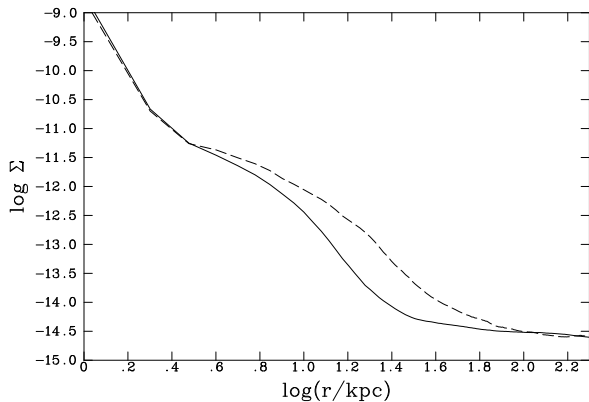


Figure 14. Comparison of the surface brightness profiles for runs with an increased halo extent (dotted line) and an increased mass replenishment rate (solid line) after 2 Gyr in units of $\text{erg s}^{-1} \text{cm}^{-2} \text{arcmin}^{-2}$.

Table 2. Wake luminosities during the first cluster crossing when the galaxy velocity is maximal (i.e. at core passage).

Run	$\log(L_X)$
Canonical	40.9
Larger halo	41.3
Smaller halo	40.4
Larger mass replenishment rate	40.9
Smaller mass replenishment rate	40.9
Larger galaxy	40.9
Smaller galaxy	40.6
Larger infall amplitude	39.9
Smaller infall amplitude	40.4

X-ray emission. However, they should be treated with caution as they do not include the effects of detector sensitivity, spatial resolution and background levels. Flux maps, such as those in Fig. 15, may be converted to simulated X-ray images as shown in Fig. 16. These simulated images represent

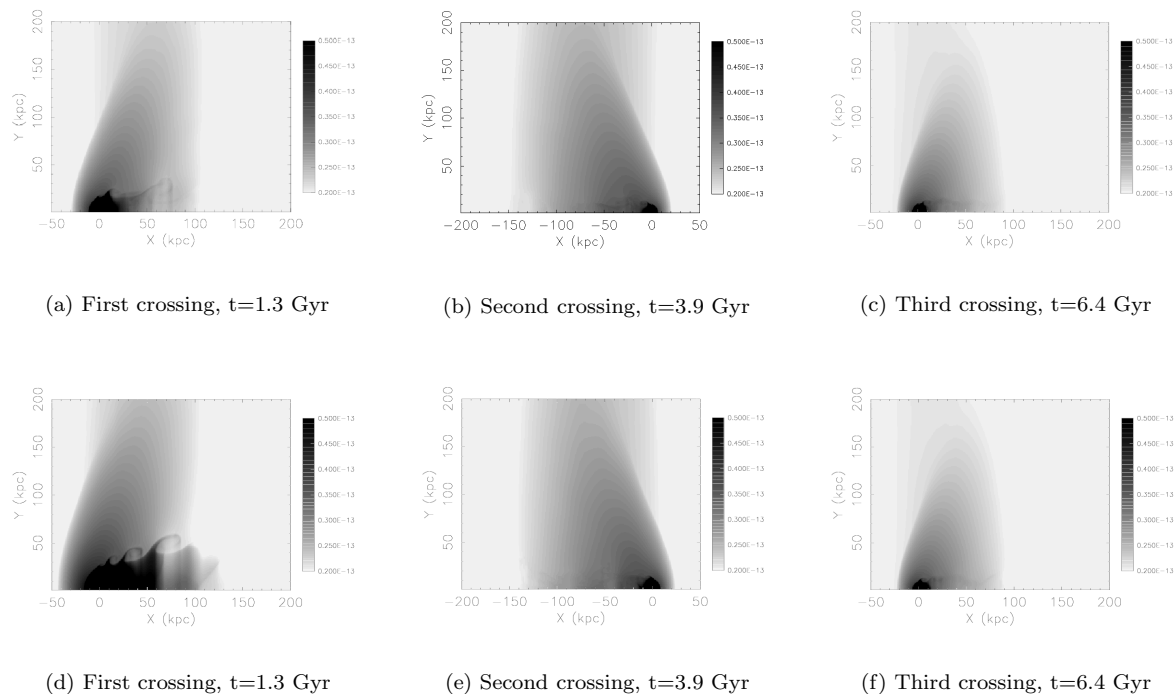


Figure 15. Simulated X-ray flux maps from the canonical run (top) and the larger gas halo run (bottom). All images are plotted using the same logarithmic greyscale in units of $\text{erg s}^{-1} \text{cm}^{-2} \text{arcmin}^{-2}$.

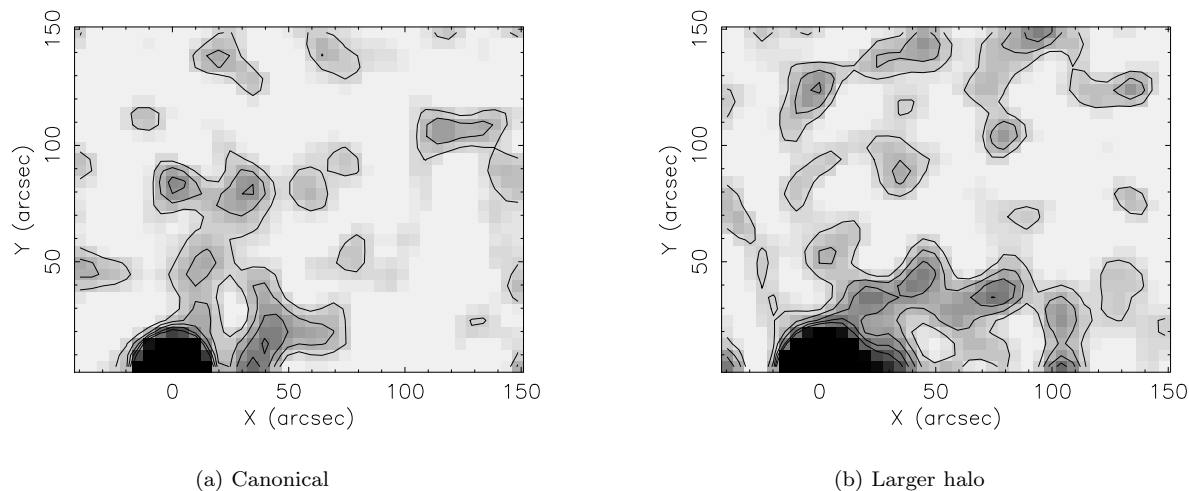


Figure 16. Significance levels in simulated X-ray images derived using the flux maps show in Fig. 15(a) and Fig. 15(d). In both cases the galaxy is at its first core passage, after 1.3 Gyr of simulated infall. Contours represent significance and are at levels of 1,2,3,4,5 σ .

50 ksec Chandra observations of the canonical galaxy at first core passage (based on the flux map in Fig. 15(a)) and the galaxy with a larger initial halo, also at first core passage (based on the flux map in Fig. 15(d)). In both cases the cluster is placed at a distance of 270 Mpc. An energy band of 0.8–2.0 keV is used to increase the contrast between the cooler galaxy emission and the hotter cluster background. The spatial bins are 5 arcsec square and $1 \text{kpc} = 0.76 \text{arcsec}$ at the assumed distance of 270 Mpc. The effects of detector background and Poisson noise have been added, a cluster

background level is then subtracted and the resulting image smoothed with a Gaussian filter of 3 pixels FWHM. Even at this relatively large distance a tail of material is visible in both cases, most prominently in the larger halo case, although it is affected by noise in the outer regions. These simulated images confirm the observability of the structures seen in the flux maps: the galaxy halo is the most observable feature, the stripped wake is the next brightest structure (with observability declining with increasing distance

from the galaxy) and the bow shock is the least observable feature, but may still be detectable.

A simple statistical measure of the degree of asymmetry present in the galaxy's X-ray halo can be formed using skewness

$$\gamma = \frac{1}{F_T \sigma^3} \sum_{i,j} F_{i,j} (x_{i,j} - \bar{x})^3 \quad (19)$$

$$\sigma^2 = \frac{1}{F_T} \sum_{i,j} F_{i,j} (x_{i,j} - \bar{x})^2 \quad (20)$$

where i and j are indices representing cells along the x and y axes respectively, $F_{i,j}$ is the flux from an individual cell, F_T is the total flux from the image, $x_{i,j}$ is the location of the cell along the x -axis and \bar{x} is the x location of the galaxy centre along the x -axis. The time variation of the skewness parameter γ , for the larger halo simulation is plotted in Fig. 17(a). This has been calculated using the broad band flux maps. Skewness derived from the corresponding simulated images is plotted in Fig. 17(b) for the same run. Fig. 17(a) represents an idealised case with no noise whereas Fig. 17(b) shows the effects of noise present in real data. When the value of skewness is positive the emission is distorted to the right and the skewness is negative when the emission is distorted to the left. Skewness is, in general, a good measure of the direction of galaxy motion although when the galaxy speed is low, in the outer regions of the cluster, there are periods when the skewness does not indicate the correct direction of motion. Given a sample of galaxies from a cluster the skewness parameter will serve as a statistical indicator of the direction of motion with respect to the ICM even after the first infall phase. A sample drawn from the central regions of the cluster will preferentially select cases where the skewness measure is a reliable direction indicator. In the above examples skewness has been calculated in a circular region of radius 120 arcsec (~ 90 kpc) centred on the galaxy to approximately encompass the significant emission from any wake formed (c.f. Fig. 15(d)). When applying skewness to real data the reliability of the measure may be enhanced by tuning the size of the region used relative to the extent of galactic haloes seen in the observation.

3.5 Shock properties

The density and temperature jumps across a shock, such as that which precedes the galaxy during supersonic motion, can be derived from the Rankine-Hugoniot relations (Landau & Lifshitz 1959),

$$\frac{\rho_2}{\rho_1} = \frac{(1 + \gamma) M_1^2}{2 + (\gamma - 1) M_1^2} \quad (21)$$

$$\frac{T_2}{T_1} = \frac{2\gamma M_1^2 - \gamma + 1}{\gamma + 1} \frac{\rho_1}{\rho_2} \quad (22)$$

where $\gamma = 5/3$ for the monatomic gas considered here. The density ratio across the shock front, present after 1.6 Gyr, is measured to be 2.0 (see Fig. 18(a)) which indicates that the Mach number of the incident gas is ~ 1.7 . The local gas temperature in the region immediately upstream of the shock is $\sim 2.6 \times 10^7$ K (see Fig. 11(d)) indicating that the gas velocity immediately upstream of the shock is ~ 1330 km s $^{-1}$, consistent with the velocity profile in Fig. 18(b). The predicted

temperature ratio across the shock is 1.8 consistent with that observed in Fig. 11(d). The velocity and Mach number derived above are local values which pertain to the region immediately upstream of the shock. The galaxy is a gravitating body and causes gas upstream to accelerate towards the shock location hence the velocity of the gas calculated above is higher than the global velocity of the galaxy with respect to the host cluster. Additionally there is a decrease in the local gas temperature during the acceleration towards the shock which also causes the Mach number to increase above the global value. In the above example the velocity of the galaxy with respect to the host cluster is 943 km s $^{-1}$ but the value derived from the density jump is 1330 km s $^{-1}$.

4 STRIPPING IN A LARGER CLUSTER

The parameter study of a number of scenarios in the same modest cluster yields information about how a homogeneous sample of wakes may be biased. However, it is also instructive to investigate the effect of placing the model galaxy in a more substantial cluster where stripping is expected to be more effective. Thus we performed a simulation with the canonical galaxy placed in a cluster with the cluster temperature scaled up by a factor of 2 to 5.4 keV. Several parameters had to be scaled accordingly, so that the cluster remains realistic. The scaled values are shown in Table 3. We scale the cluster velocity dispersion σ_c , the cluster core radius r_c and the central ICM density n_{ICM} as follows.

$$\sigma_c \propto T^{1/2} \quad (23)$$

to be consistent with eqn. 14, and

$$r_c \propto T^{1/2} \quad (24)$$

assuming that the core radius is a fixed fraction of the virial radius and that the virial radius scales with temperature in a self similar fashion. The scaling of the central ICM density was based on the X-ray emission properties. For a beta model surface brightness distribution with $\beta = 2/3$ the central emissivity S_0 scales as

$$S_0 \propto j_0 r_c \quad (25)$$

where the central emissivity j_0 is assumed to scale as

$$j_0 \propto n_{\text{ICM}}^2 \quad (26)$$

hence

$$S_0 \propto n_{\text{ICM}}^2 r_c. \quad (27)$$

From eqn. 15

$$L_X \propto S_0 r_c^2. \quad (28)$$

Combining eqns. 27 and 28 gives

$$n_{\text{ICM}}^2 \propto L_X r_c^{-3}. \quad (29)$$

It is assumed that L_X scales as $L_X \propto T^3$ in accordance with observationally determined relations (White et al. 1997) rather than $L_X \propto T^2$ which would be expected from self similarity.

The velocity of the galaxy in the hotter cluster is plotted as the solid line in Fig. 19, and for comparison the velocity variation for the galaxy in the 2.7 keV cluster is shown by the dotted line. The cluster sound speed is shown by the

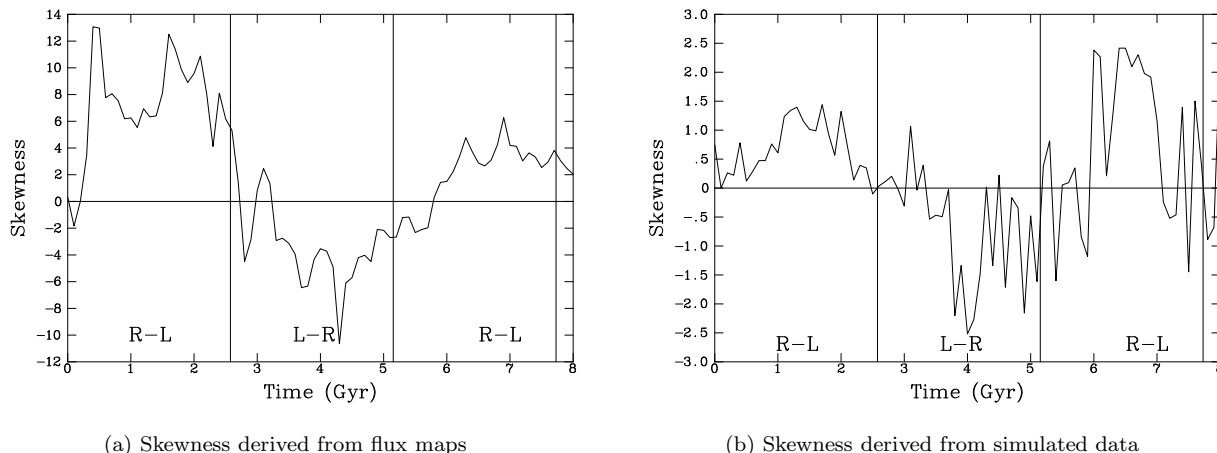


Figure 17. Time variation of skewness parameter based on the flux maps from the canonical case. The vertical lines mark regions where the galaxy motion is from right to left (R-L) or from left to right (L-R). When the skew is positive the emission is distorted to the right and when the skew is negative the distortion is to the left.

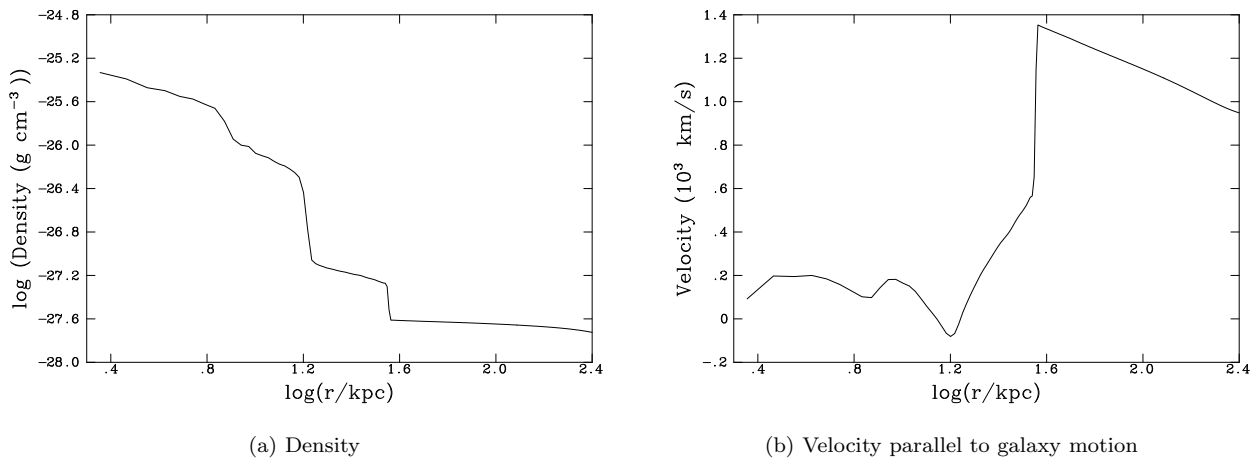


Figure 18. Density and velocity jumps across the shock after 1.6 Gyr. The both quantities are measured upstream, parallel to the direction of galaxy motion along a line through the centre of the galaxy. The galaxy is centred at $r = 0$.

Table 3. Parameters of the hotter cluster.

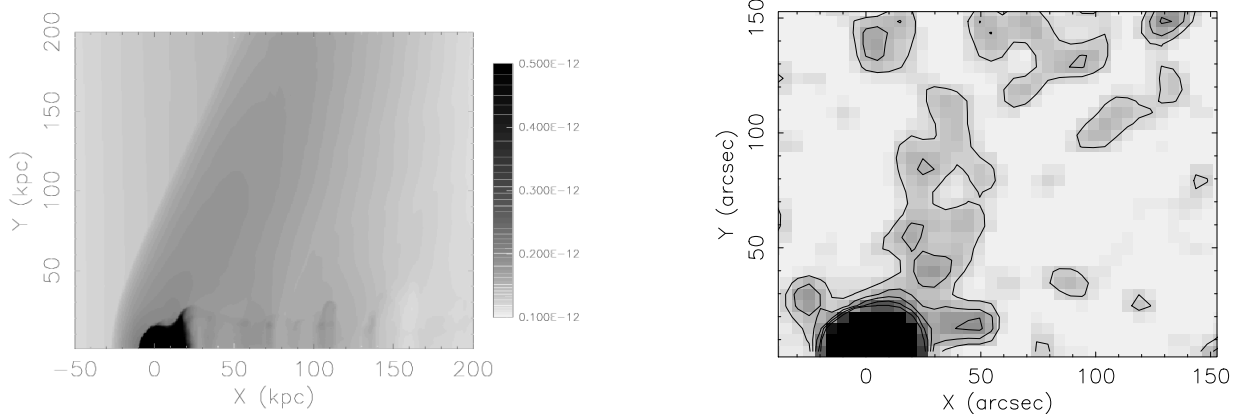
Parameter	Value
Temperature	5.4 keV
Velocity dispersion	928 km s ⁻¹
Core radius	566 kpc
Central ICM density	1.75×10^{-3} cm ⁻³

solid and dotted horizontal lines for the hotter cluster and cooler cluster respectively. The cluster crossing time is the same in both cases as galaxy velocity and cluster size both scale as $T^{1/2}$.

The mass of gas gravitationally bound to the galaxy (shown in Fig. 20) is significantly less in the hotter cluster after the first 2 Gyr. The bound gas content is initially higher

as the galactic gas halo density must increase to counteract the increased ICM pressure confinement. However, this extra gas is quickly stripped during the first crossing. The ram pressure is higher in a hotter cluster due to the higher ICM density and also due to the higher velocities reached. As a consequence it would be expected that galaxies residing in such an environment would retain less gas than those galaxies in cooler clusters where stripping is less effective.

It is expected that wakes will be more difficult to observe in hotter clusters for two reasons. Firstly, the gas content of the cluster galaxies should be rapidly depleted by stripping, and secondly the background emission from the ICM will be brighter than in a cooler system. In order to assess the observability of wakes in the hotter cluster we have again derived simulated X-ray flux maps and simulated images. These are presented in Fig. 21. The flux map



(a) Simulated X-ray flux map similar to those in Fig. 15. Note the difference in the greyscale levels used here compared to those used in Fig. 15

(b) Significance levels in a simulated X-ray image, similar those in Fig. 16. Contours represent significance and are at levels of 1,2,3,4,5 σ .

Figure 21. Simulated X-ray flux map and significance map for the hotter cluster run after 1.3 Gyr.

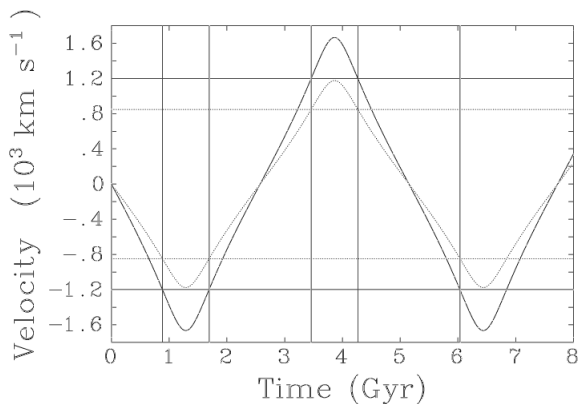


Figure 19. Velocity of the galaxy in the hotter cluster (solid line) and the 2.7 keV cluster (dotted line). Horizontal lines mark the cluster sound speed (solid line is hotter cluster, dotted line is 2.7 keV cluster). Solid vertical lines mark the transition from the subsonic to supersonic regime which is the same in both cases.

was generated in the same way as those in Fig. 15 and the significance plot was generated in the same way as Fig. 16 to enable a direct comparison between the results for the hotter and canonical clusters. The gas halo associated with the galaxy produces a significant amount of emission, as seen in Fig. 21(b), as the high initial gas content has not yet been stripped at this stage. There is a wake of emission from stripped material but it is shorter and narrower than the previous wakes in Fig. 16 indicating that wakes in hotter clusters will be less observable than in cooler systems. The bow shock may also be detectable.

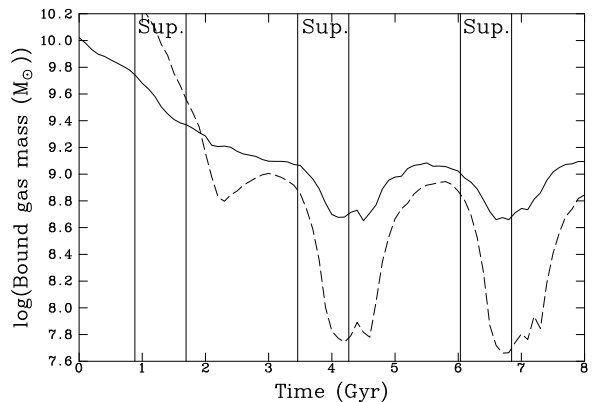


Figure 20. Mass of gas gravitationally bound to the galaxy in the canonical (solid line) and hotter cluster (dashed line) runs.

5 SUMMARY AND DISCUSSION

We present results from a parameter study involving hydrodynamic simulations of a large elliptical galaxy falling radially into an intermediate temperature cluster. The resulting stripping causes variations in the gas mass associated with the galaxy and in the resulting X-ray luminosity. Variations in model parameters (particularly mass replenishment rate) are found to induce larger variations in L_X (~ 2 dex) than the effects of observing a given model at different points during the galaxy's dynamic cycle.

The luminosity of the X-ray wake during the first cluster passage is found to be most strongly influenced by the extent of the pre-existing gas halo and during subsequent passages through the cluster there is not a bright X-ray wake. This indicates that samples of wakes in clusters will be biased towards large elliptical galaxies, with substantial haloes, which are on their first passage through the cluster. Wakes surrounding galaxies residing in hotter, more massive clusters are, as expected, less easily detected.

The infall of a cooler gas halo into a cluster results in structures reminiscent of the cold fronts seen in cluster mergers. The cold front is found to be a more prominent surface brightness feature than the shock front, present during supersonic motion, in agreement with recent Chandra results of cluster mergers. The density and temperature ratios across the shock front are found to be consistent with values from analytic theory but the velocity derived in this way is a local value which differs from the global velocity of the galaxy with respect to the cluster potential as the galaxy is a gravitating body which accelerates the local ICM. Surface brightness enhancements and temperature variations arising from the galaxy motion should be detectable with present instrumentation such as Chandra and XMM.

ACKNOWLEDGEMENTS

DMA acknowledges funding from a Postgraduate Teaching Assistantship from the School of Physics & Astronomy, while IRS and IS acknowledge funding from PPARC. We would like to thank an anonymous referee for helpful comments.

REFERENCES

- Balsara D., Livio M., O’Dea C. P., 1994, *ApJ*, 437, 83
 Bender R., Burstein D., Faber S. M., 1993, *ApJ*, 411, 153
 Blondin J. M., Fryxell B. A., Konigl A., 1990, *ApJ*, 360, 370
 Brüggén M., Hillebrandt W., 2001a, *MNRAS*, 320, 73
 Brüggén M., Hillebrandt W., 2001b, *MNRAS*, 323, 56
 Brighenti F., Mathews W. G., 1998, *ApJ*, 495, 239
 Brown B. A., Bregman J. N., 2000, *ApJ*, 539, 592
 Bullock J. S., Kolatt T. S., Sigad Y., Somerville R. S., Kravtsov A. V., Klypin A. A., Primack J. R., Dekel A., 2001, *MNRAS*, 321, 559
 Cappellaro E., Turatto M., Benetti S., Tsvetkov D. Y., Bartunov O. S., Makarova I. N., 1993, *A&A*, 273, 383
 Ciotti L., Pellegrini S., Renzini A., D’Ercole A., 1991, *ApJ*, 376, 380
 Colella P., Woodward P. R., 1984, *J. Comp. Phys.*, 54, 174
 Drake N., Merrifield M. R., Sakelliou I., Pinkney J. C., 2000, *MNRAS*, 314, 768
 Dressler A., 1980, *ApJ*, 236, 351
 Faber S. M., Jackson R. E., 1976, *ApJ*, 204, 668
 Finoguenov A., Jones C., 2000, *ApJ*, 539, 603
 Forman W., Schwarz J., Jones C., Liller W., Fabian A. C., 1979, *ApJL*, 234, L27
 Gaetz T. J., Salpeter E. E., Shaviv G., 1987, *ApJ*, 316, 530
 Irwin J. A., Sarazin C. L., 1996, *ApJ*, 471, 683
 Kent S. M., Gunn J. E., 1982, *AJ*, 87, 945
 Landau L. D., Lifshitz E. M., 1959, *Fluid Mechanics*. Pergamon
 Lauer T. R., 1985, *ApJ*, 292, 104
 Markevitch M., Ponman T. J., et al. 2000, *ApJ*, 541, 542
 Matsushita K., Ohashi T., Makishima K., 2000, *PASJ*, 52, 685
 Merrifield M. R., 1998, *MNRAS*, 294, 347
 Mori M., Burkert A., 2000, *ApJ*, 538, 559
 Navarro J. F., Frenk C. S., White S. D. M., 1997, *ApJ*, 490, 493
 Neumann D. M., Arnaud M., Gastaud R., Aghanim N., Lumb D., Briel U. G., Vestrand W. T., Stewart G. C., Molendi S., Mittaz J. P. D., 2001, *A&A*, 365, L74
 Neumann D. M., Lumb D. H., Pratt G. W., Briel U. G., 2002, *astro-ph/0212432*
 O’Sullivan E., Forbes D. A., Ponman T. J., 2001, *MNRAS*, 328, 461
 Paolillo M., Fabbiano G., Peres G., Kim D.-W., 2002, *ApJ*, 565, 883
 Rangarajan F. V. N., White D. A., Ebeling H., Fabian A. C., 1995, *MNRAS*, 277, 1047
 Richards M. T., Ratliff M. A., 1998, *ApJ*, 493, 326
 Stevens I. R., Acreman D. M., Ponman T. J., 1999, *MNRAS*, 310, 663
 Strickland D. K., Stevens I. R., 2000, *MNRAS*, 314, 511
 Takeda H., Nulsen P. E. J., Fabian A. C., 1984, *MNRAS*, 208, 261
 Toniazzo T., Schindler S., 2001, *MNRAS*, 325, 509
 Tully R. B., 1987, *ApJ*, 321, 280
 Vikhlinin A., Markevitch M., Murray S. S., 2001a, *ApJ*, 551, 160
 Vikhlinin A., Markevitch M., Murray S. S., 2001b, *ApJL*, 549, L47
 White D. A., Fabian A. C., Forman W., Jones C., Stern C., 1991, *ApJ*, 375, 35
 White D. A., Jones C., Forman W., 1997, *MNRAS*, 292, 419